


Using Thermal Crowding to Direct Pattern Formation on the Nanoscale

Ryan Allaire 

Department of Mathematical Sciences, United States Military Academy, West Point, New York 10996, USA

Linda J. Cummings  and Lou Kondic 

Department of Mathematical Sciences, New Jersey Institute of Technology, Newark, New Jersey 07102, USA

 (Received 23 May 2024; revised 15 October 2024; accepted 23 October 2024; published 21 November 2024)

Metal films and other metal geometries of nanoscale thickness deposited on an insulating substrate, when exposed to laser irradiation, melt and evolve as fluids as long as their temperature is sufficiently high. This evolution often leads to pattern formation, which may be influenced strongly by material parameters that are temperature dependent. In addition, the laser heat absorption itself depends on the time-dependent metal thickness. Self-consistent modeling of evolving metal films shows that, by controlling the amount and geometry of the deposited metal, one can control the instability development. In particular, we demonstrate the “thermal crowding” effect: additional metal leads to elevated temperatures, which strongly influence the metal evolution, even if the metal geometries are disjoint. We demonstrate that the communication of disjoint metal domains occurs via heat diffusion through the underlying substrate. Fully self-consistent modeling focusing on the dominant effects, as well as accurate time-dependent simulations, allow us to describe the main features of thermal crowding and provide a route to control fluid instabilities and pattern formation on the nanoscale.

DOI: [10.1103/PhysRevLett.133.214003](https://doi.org/10.1103/PhysRevLett.133.214003)

Introduction—Self-assembly and directed assembly has been the topic of numerous recent works, in particular for nanoscale fluid-based systems [1,2]. While in many cases self-assembly can be used to produce patterns of interest, often directed assembly is needed to achieve desired outcomes such as, for example, an ordered array of nanoparticles. Systems involving metal films, filaments, and other geometries of nanoscale thickness are of particular current interest due to the large number of applications involving plasmonics, of relevance to solar cells, catalysis, and biomedical applications, etc., as reviewed by many authors [3–8]. Such metal geometries are commonly exposed to short-duration (tens of nanoseconds) laser pulses to bring the material above the melting point. While molten, metals evolve as (to a first approximation, Newtonian) fluids, but with strongly temperature-dependent material properties, and are subject to fluid-dynamical instabilities. Such instabilities, which evolve on a timescale comparable to that of the applied laser pulses, may lead to the formation of drops (becoming particles upon solidification). The size and placement of such particles are of crucial importance in applications, and it is important to be able to control them.

Directed assembly has been explored in the past using elaborately designed initial metal geometries obtained, for example, by lithographically imposing sinusoidal perturbations to a metal strip to produce a desired outcome [9]. This method, while ingenious, is costly and may not be practical. In this Letter we show that pattern formation can

be controlled indirectly, via thermal transport through the supporting substrate. We call this approach to directed assembly “thermal crowding” since, as we will show, adjacent (though disconnected) metal geometries experience each other through thermal contact. Therefore, simply by modifying the initial size and placement of simple metal structures such as filaments, one can direct the evolution and obtain patterns with desired properties.

Model—Modeling nanoscale metal films and other geometries exposed to laser irradiation is challenging, since multiple physical effects must be included, particularly regarding the coupling of thermal effects due to the laser heating (including phase change) with fluid dynamics. Our previous work in this area [10–12], which extended other research efforts, see, e.g., [13–16], constitutes a self-consistent and asymptotically accurate framework for this complex problem. The resulting set of equations, governing the thermal transport and the metal film evolution while molten, is discretized and solved in a graphical processing unit-based computing environment, using our open-source, publicly available code [17]. Our particular focus is on evolving metal filaments of various sizes; such simple geometry illustrates the importance of careful coupling of the fluid dynamics with thermal transport and provides a straightforward proof of principle of using the initial configurations of simple metal shapes to control the final droplet (nanoparticle) size and number. In what follows, we outline the main features of the theoretical and computational methods that we use and direct the interested reader

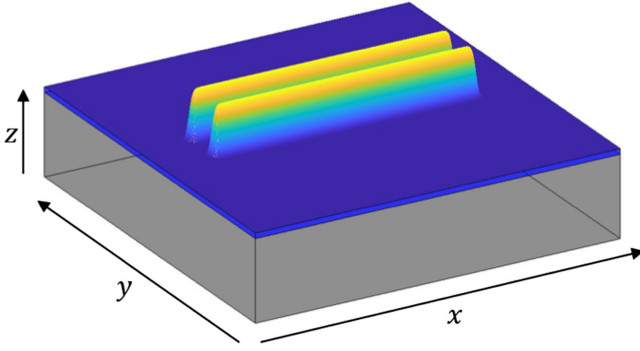


FIG. 1. Schematic of two neighboring filaments (both indicated by the color gradient, with yellow representing maximum height) and thinner equilibrium film region (dark blue). The gray region represents the underlying SiO₂ substrate. In physical experiments [20], the in-plane dimensions are measured in hundreds of nanometers, the typical metal thickness is 10–20 nm, and the substrate (membrane) thickness is on the order of 100 nm.

to Supplemental Material [18] and our earlier works [11,12] for the details, including, in particular, the careful asymptotic expansion of the governing equations that leads to the formulation presented here.

Consider a free surface metal filament of characteristic nanoscale thickness $H = 10$ nm, which we will use as a length scale. Suppose further that the metal is initially solid, exposed to air above, and in contact below with a thermally conductive solid SiO₂ substrate of depth H_s , see Fig. 1. Following [11], we choose the velocity scale $U = \gamma_f / (3\mu_f)$ (where γ_f and μ_f are surface tension and viscosity at melting temperature, T_{melt}), leading to the timescale, H/U . Subsequently, we choose T_{melt} , $\mu_f U/H$, and γ_f as the temperature, pressure, and surface tension scales, respectively. We note that the specified choices emphasize the capillary and viscous forces; alternative formulations are possible (see Ref. [19] for details).

Once in the liquid state, we treat the metal as an incompressible Newtonian fluid. The most complete model consists of the Navier-Stokes equations for the molten metal film, coupled with heat equations for the metal and substrate, plus appropriate boundary conditions and constitutive equations for the temperature-dependent material parameters. We assume that metal viscosity depends on temperature, but that the surface tension, density, heat capacity, and thermal conductivity are fixed at their melting temperature values (see Supplemental Material, Sec. VI [18] for discussion of the temperature dependence of surface tension, and prior work [12] for that of thermal conductivity). Note in particular that the model allows for both spatial and temporal dependence of viscosity through the dependence of this material parameter on the temperature field. We use T_f , T_s to denote the film and substrate temperatures, respectively, and define $T_{\text{avg}}(t)$ to be the time-dependent spatially averaged filament temperature (see Sec. V of [18] for a complete definition). For the

remainder of the text, we omit the argument of $T_{\text{avg}}(t)$ with the understanding that it is time dependent.

In recent work [11,12] we proposed a simplified model for this setup based on a long-wave formulation for a thin metal geometry. The metal film thickness [$z = h(x, y, t)$ where x and y are the in-plane coordinates] evolution is governed by the following fourth order nonlinear partial differential equation

$$\partial_t h + \nabla_2 \cdot \left[\frac{1}{\mu(T_f)} h^3 \nabla_2 (\nabla_2^2 h + \Pi(h)) \right] = 0 \quad (1)$$

(see Supplemental Material, Sec. II [18] for the reduction to this nondimensional form), where $\nabla_2 = (\partial_x, \partial_y, 0)$. Following the time derivative term in Eq. (1) are the capillary and disjoining pressure (modeling liquid-solid interaction) terms; $\mu(T_f)$ is the temperature-dependent viscosity (scaled by μ_f), modeled via an Arrhenius-type relationship (see Supplemental Material, Sec. IV [18] for details).

The model specified by Eq. (1) has been considered extensively in the context of filament breakup under isothermal conditions (hence constant viscosity), often with additional effects such as gravity, to describe the breakup of macroscopic infinite length [21,22] and finite-length filaments [19]; see also Supplemental Material, Sec. I [18] and Refs. [23–28]. Both linear stability analysis of the isothermal problem, and numerical simulations, show that the distance between the drops that form on breakup (as well as their size) is determined by the filament cross-sectional area, while the instability mechanism itself is governed by the interplay between capillary effects and the destabilizing liquid-solid interaction forces specified by $\Pi(h)$, whose range is comparable to the film thickness [29]. (Analytical progress via linear stability analysis is not possible for the nonisothermal case.) We use $\Pi(h) = \Omega[(h_*/h)^n - (h_*/h)^m]$, with equilibrium film thickness h_* , constant Ω [related to the Hamaker constant A_H by $\Omega = A_H / (6\pi\gamma_f h_*^3 H^2)$], and exponents $n > m > 1$, see, e.g., [10]. Such a conjoining-disjoining form ensures that the film height approaches a minimum value comparable to h_* as dewetting proceeds (we typically use $h_* = 0.1$, corresponding to 1 nm; while this value is larger than that expected in experiments [30], this choice avoids the numerically more expensive simulations that are required for smaller values of h_* , while having negligible effect on the fluid dynamics). Interfacial potentials for liquid metals are undoubtedly more complex (and may be temperature dependent [31]), however, based on our earlier work and on comparison to experiment [30], we expect that the present form is sufficient for our purposes.

The heat flow model we developed recently [11] exploits further the long-wave approximation. The metal has much higher thermal conductivity than the substrate, and the temperature variation across the film (in the short, z

direction) may be shown to be weak. We retain those assumptions here, but in contrast to our earlier work (and justified below), we assume that in-plane heat conduction in the substrate may be relevant, and that heat is lost from the system only through the lateral substrate boundaries. This leads to the following system governing temperature

$$h\text{Pe}_f\partial_t T_f = \nabla_2 \cdot (h\nabla_2 T_f) - \mathcal{K}\partial_z T_s|_{z=0} + h\bar{Q}, \quad (2)$$

$$\text{Pe}_s\partial_t T_s = \nabla_2^2 T_s + \partial_z^2 T_s, \quad (3)$$

for the metal and for the substrate, respectively. The boundary conditions (BCs) include continuity of temperature at $z = 0$ [continuity of heat flux was already imposed in deriving (2) and (3)] and appropriate BCs at the domain boundaries: $T_f = T_s$ at $z = 0$, $\partial_z T_s = 0$ at $z = -H_s$, $\partial_x T_f = 0$ at $x = 0, P$, $\partial_y T_f = 0$ at $y = 0, P$, and $T_s = T_a$ (ambient temperature) at $x = 0, P$, $y = 0, P$ ($P = 140$). The parameters, defined by

$$\text{Pe}_f = \frac{(\rho c)_f UH}{k_f}, \quad \text{Pe}_s = \frac{(\rho c)_s UH}{k_s}, \quad \mathcal{K} = \frac{k_s}{k_f},$$

represent the film and substrate Péclet numbers, and thermal conductivity ratio, respectively. Equation (2) describes the leading order fluid temperature; the terms on the right-hand side represent the in-plane diffusion, heat loss to the substrate, and the depth-averaged laser heating (see Refs. [13,32] and the references therein for more details on the form of this term)

$$\bar{Q} = \frac{A(h)}{h} \int_0^h F(t)[1 - R(h)] \exp[-\alpha_f(h - z)] dz. \quad (4)$$

Here, α_f^{-1} is the absorption length for laser radiation in the metal film and $F(t)$ captures the temporal dependence of the laser pulse, taken to be Gaussian centered at a specified time t_p and of prescribed width σ (corresponding to tens of nanoseconds). The factor $A(h)$ is a smooth approximation of $\mathcal{U}(h - h_*)$, the unit step function centered at h_* , which turns off absorption as $h \rightarrow h_*$. In-plane diffusion is also turned off as $h \rightarrow h_*$, ensuring that the filaments alone absorb energy and transfer heat to other filaments only via the substrate (these adjustments are needed due to the unphysically large value chosen for h^* , which would otherwise lead to measurable, though spurious, heat transport through the precursor). In general, the reflectivity of the film on a transparent substrate $R(h)$ is determined by Maxwell's equations [33], but the resultant form is cumbersome; following others [13,32] we approximate it by $R(h) = r_0[1 - \exp(-\alpha_r h)]$, where parameters r_0 and α_r are chosen to ensure good agreement with the exact solution.

Equation (3) describes the substrate heat conduction. The BCs on Eqs. (2) and (3) impose no heat loss at the bottom of the substrate (motivated by the experiments on

thin substrates (membranes) discussed below), and insulating conditions for the metal at its lateral boundaries. We impose room temperature at the lateral boundaries of the substrate, leading to the only heat loss mechanism. The no-heat-loss BC at the bottom of the substrate motivates the inclusion of in-plane thermal flow in Eq. (3); heat flow in the z direction is negligible. Additional assumptions used to derive the fluid dynamical and thermal models can be found in Supplemental Material, Sec. V [18] and Refs. [12,13,32,34–36].

Results—We focus on setups relevant to recent experiments [37] involving nanoparticle formation on so-called “membranes.” Membranes are essentially very thin solid substrates with overlaid nanoscale metal patterns, obtained by combining lithographic techniques with chemical etching of the underlying silicon [37]. An important motivation for using membranes is that one can observe not only the final outcome of experiments, but also the time evolution, since membranes are optically transparent and allow for the use of dynamic transmission electron microscopy, which provides unique nanosecond temporal and nanometer spatial resolution [37]. From the modeling perspective, the key point is that the bottom boundary of the substrate is strongly insulating; the membrane setup allows for precise control of heat flow. [While carrying out experiments on (thick) SiO_2 wafers requires more energy, the model discussed here describes such experiments accurately as well; see Ref. [12] for details.]

In our simulations, the initial condition is a metal filament, or several filaments at a specified distance apart, with the exact geometry specified in Supplemental Material, Sec. III [18]. Initially, both metal and substrate are at room temperature. Then, the laser pulse is applied, the metal temperature increases (discussed more precisely in what follows), and when the filament temperature rises above the melting point, it starts evolving as a Newtonian fluid. When the laser energy begins to decrease, the filament temperature decreases as well, and once it drops below the melting temperature, the evolution stops. The simulations are carried out using our in-house graphical processing unit-based code [17]. The computational method itself is based on finite difference spatial discretization, combined with Crank-Nicolson temporal evolution within an alternate direction implicit framework; see Ref. [12] for details. The parameters used in all simulations are provided in Supplemental Material, Table 1 [18].

Figures 2(a) and 2(b) show the results of two sets of simulations, whose only difference is the number of filaments present. Still, the final outcome is very different. While in both cases the filament melts, for this choice of parameters no significant instability development occurs in (a) prior to resolidification, whereas in (b) the evolution is much more advanced, exhibiting a pearling type of instability, with the distance and size of the droplets determined by the filament size and the underlying interplay between

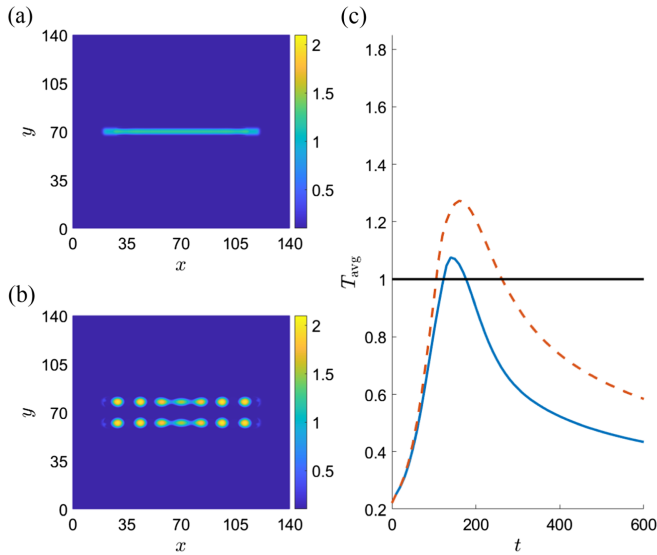


FIG. 2. Final configuration of (a) a single metal filament and (b) two metal filaments placed at a distance of $D = 15$ apart, exposed to the same laser pulse. Frame (c) shows the maximum temperatures for the configurations in (a) (blue solid line) and (b) (red dashed line), along with the melting line (black). See also Animation 1 in Supplemental Material [18] for fluid evolution and temperature fields.

capillary and liquid-solid interaction forces [19,21,38]. Figure 2(c) shows why: the average temperature is significantly higher in the case of two filaments, and furthermore, the metal temperature in this case remains above melting for a longer time. Because of the Arrhenius-type dependence of viscosity on temperature, the evolution is also faster when multiple filaments are present. Animation 1 in Supplemental Material [18] shows the time and space dependence of the film and temperature evolution; note that filaments cool faster toward their ends. The animation also emphasizes the significantly higher temperature attained for two filaments compared to one, leading to the faster evolution and breakup noted above. We remark that the details of the final outcome depend on the choice of parameters, including the filaments' volume and aspect ratio, see Supplemental Material, Secs. VII and VIII [18]; the concept of thermal crowding (higher temperatures in the presence of additional metal) is, however, always found to hold, with faster evolution and breakup for multiple filaments.

Figure 3 shows the effect that the number of filaments and their respective spacing has on the collective heating and dewetting, illustrating that thermal crowding can strongly influence filament evolution. The comparison of different rows shows that an increase in the number of filaments strongly influences their temperatures and, through the temperature-dependent viscosity, the resultant dewetting. For example, in Fig. 3(b) the filaments melt, but not sufficiently even to dewet partially; whereas the filaments in Figs. 3(e) and 3(h) both show full dewetting

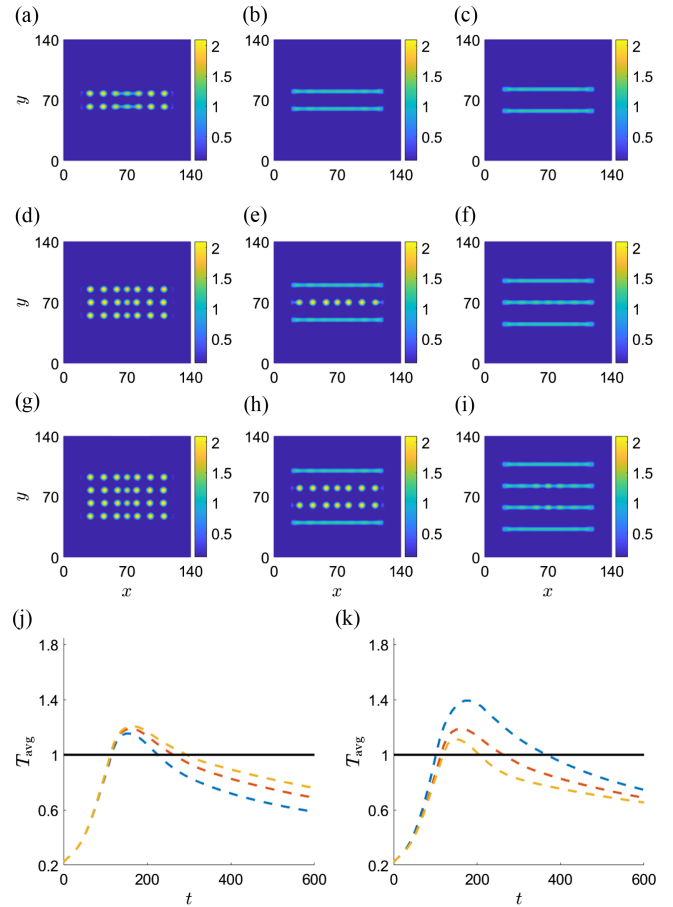


FIG. 3. (a)–(i) Final configuration of two (row 1), three (row 2), and four filaments (row 3) at distances $D = 15$ (column 1), $D = 20$ (column 2), $D = 25$ (column 3). (j) Time evolution of the average film temperature for (b) blue dashed line, (e) orange dashed line, and (h) yellow dashed line. (k) Time evolution of the average film temperature for (d) blue dashed line, (e) orange dashed line, and (f) yellow dashed line. The melting temperature T_{melt} is shown by the solid black line. See also Animations 2 and 3 in Supplemental Material [18].

of the interior filaments. Interestingly, the filaments that are farthest from the center only begin undulation growth before they freeze in place because they only receive one-sided diffusive heating from the other filaments. The interior filaments of Figs. 3(e) and 3(h) then spend more time in the liquid phase, are hotter, of lower viscosity, and therefore evolve faster than the outermost filaments; see also Animation 2 in Supplemental Material [18]. This simulation also illustrates the relevance of both the number of filaments and their spacing; in the particular case considered here, the distance between filaments is more important since the configuration in Fig. 3(d) (three filaments at spacing $D = 15$) remains hot longer than that in Fig. 3(h) (four filaments at spacing $D = 20$), consistent with the information on average temperatures provided by Figs. 3(j) and 3(k).

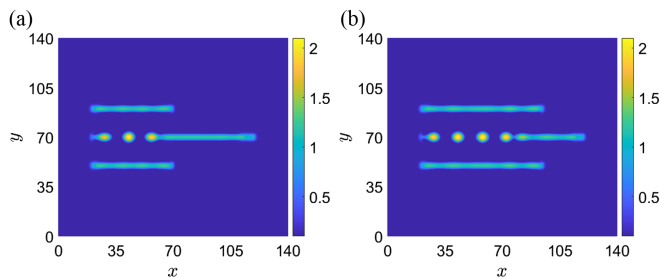


FIG. 4. Asymmetric configuration of a filament of length 100 surrounded by two filaments of lengths 50 (a) and 75 (b) at a distance $D = 20$. See also Supplemental Material, Animation 4 [18].

There are two possible reasons for the unbalanced heating leading to a breakup of internal filaments only: (i) loss of heat through the domain boundaries, and (ii) decreased heating of the external filaments by the internal ones. Insight regarding which of these mechanisms is most relevant can be gained by carrying out simulations on larger domains. These additional results, see Supplemental Material Sec. VI [18], show that the influence of heat loss through domain boundaries is minimal, and therefore, one-sided heating governs the evolution and breakup.

Figure 3(j) shows that increasing the number of filaments, while keeping their spacing fixed, has a fairly modest effect on the maximum metal temperature; but a larger number of filaments collectively retains heat for longer, leading to increased liquid lifetimes and more complete dewetting. Figure 3(k) shows that increasing the interfilament distance D leads to lower filament temperatures. In particular, placing three filaments at a distance $D = 15$ [Fig. 3(d)] is sufficient to collectively melt and fully evolve all three into nanoparticles, as opposed to placing them at distance $D = 25$ [Fig. 3(f)], which (although the filaments melt) is insufficient to produce any nanoparticle formation. Additional information regarding spatial temperature distribution is available in Supplemental Material, Animation 3 [18], which reveals the temperature maxima to occur at the center of the domain, with lower temperatures toward the periphery, consistent with, e.g., the results shown in Fig. 3(i), where the central filaments exhibit better-developed undulations toward the filament centers.

Figure 4 illustrates that filament instability can be initiated asymmetrically and the number of droplets can be controlled accordingly. Here, we surround a filament of length 100 on both sides by filaments of lengths 50 (a) and 75 (b). The presence of the additional short filaments is sufficient to increase the temperature of the left side of the long filament and induce breakup; and the number and location of droplets can be subsequently controlled by increasing the outer filament length and location. The short filaments themselves melt; however, asymmetric one-sided heating is insufficient for their complete breakup.

Additionally, Supplemental Material, Animation 4 [18] shows that the leftmost droplet solidifies prior to fully dewetting, illustrating the nontrivial competition between the edge retraction and the resolidification. Additional examples of more elaborate filament configurations are given in Supplemental Material, Secs. IX and X [18] we also show an example of evolution as a result of application of multiple laser pulses.

Conclusions—We have illustrated a simple but powerful method that allows for the coupling of fluid dynamics and heat transport for metal filaments deposited on thermally conductive substrates. Our approach is fully self-consistent, with fluid dynamics influencing and being influenced by the heat flow. This coupling occurs through temperature dependence of metal viscosity, whose spatial variation influences the fluid thickness and, in turn, the amount of heating absorbed. In the present work, we apply this method to metal filaments of nanoscale thickness; however, the concept of thermal crowding may be relevant for different materials and across different geometries and length scales. In the context of metals, our results open the door to various directed- and self-assembly approaches since it is now possible to control the dynamics simply by specifying the initial material distribution.

Acknowledgments—This research was supported by NSF DMS-1815613, an NJIT seed grant (2022), and a USMA Dean’s Faculty Research Fund. Helpful discussions with Professor Philip Rack (UT Knoxville) are also acknowledged.

- [1] M. Grzelczak, J. Vermant, E. M. Furst, and L. M. Liz-Marzán, Directed self-assembly of nanoparticles, *ACS Nano* **4**, 3591 (2010).
- [2] Z. Chai, A. Childress, and A. A. Busnaina, Directed assembly of nanomaterials for making nanoscale devices and structures: Mechanisms and applications, *ACS Nano* **16**, 17641 (2022).
- [3] H. Atwater and A. Polman, Plasmonics for improved photovoltaic devices, *Nat. Mater.* **9**, 205 (2010).
- [4] D. Wang and Y. Li, Bimetallic nanocrystals: Liquid-phase synthesis and catalytic applications, *Adv. Mater.* **23**, 1044 (2011).
- [5] R. G. Chaudhuri and S. Paria, Core/shell nanoparticles: Classes, properties, synthesis mechanisms, characterization, and applications, *Chem. Rev.* **112**, 2373 (2012).
- [6] S. V. Makarov, V. A. Milichko, I. S. Mukhin, I. I. Shishkin, D. A. Zuev, A. M. Mozharov, A. E. Krasnok, and P. A. Belov, Controllable femtosecond laser-induced dewetting for plasmonic applications, *Laser Photonics Rev.* **10**, 91 (2016).
- [7] R. A. Hughes, E. Menumorov, and S. Neretina, When lithography meets self-assembly: A review of recent advances in the directed assembly of complex metal nanostructures on planar and textured surfaces, *Nanotechnology* **28**, 282002 (2017).

- [8] F. Ruffino and M. G. Grimaldi, Nanostructuring of thin metal films by pulsed laser irradiations: A review, *Nanomater. Nanotechnol.* **9**, 1133 (2019).
- [9] J. D. Fowlkes, L. Kondic, J. A. Diez, and P. D. Rack, Self-assembly versus directed assembly of nanoparticles via pulsed laser induced dewetting of patterned metal films, *Nano Lett.* **11**, 2478 (2011).
- [10] L. Kondic, A. G. González, J. A. Diez, J. D. Fowlkes, and P. Rack, Liquid-state dewetting of pulsed-laser-heated nanoscale metal films and other geometries, *Annu. Rev. Fluid Mech.* **52**, 235 (2020).
- [11] R. H. Allaire, L. J. Cummings, and L. Kondic, On efficient asymptotic modelling of thin films on thermally conductive substrates, *J. Fluid Mech.* **915**, A133 (2021).
- [12] R. H. Allaire, L. J. Cummings, and L. Kondic, Influence of thermal effects on the breakup of thin films of nanometric thickness, *Phys. Rev. Fluids* **7**, 064001 (2022).
- [13] J. Trice, D. Thomas, C. Favazza, R. Sureshkumar, and R. Kalyanaraman, Pulsed-laser-induced dewetting in nanoscopic metal films: Theory and experiments, *Phys. Rev. B* **75**, 235439 (2007).
- [14] A. Atena and M. Khenner, Thermocapillary effects in driven dewetting and self assembly of pulsed-laser-irradiated metallic films, *Phys. Rev. B* **80**, 075402 (2009).
- [15] F. Saeki, S. Fukui, and H. Matsuoka, Thermocapillary instability of irradiated transparent liquid films on absorbing solid substrates, *Phys. Fluids* **25**, 062107 (2013).
- [16] S. Shklyaev, A. A. Alabuzhev, and M. Khenner, Long-wave Marangoni convection in a thin film heated from below, *Phys. Rev. E* **85**, 016328 (2012).
- [17] R. H. Allaire, Gadit thermal, https://github.com/Ryallaire/GADIT_THERMAL (2021).
- [18] See Supplemental Material at <http://link.aps.org/supplemental/10.1103/PhysRevLett.133.214003> for details regarding parameters, initial conditions, supporting results, and animations.
- [19] J. A. Diez, A. González, and L. Kondic, On the breakup of fluid rivulets, *Phys. Fluids* **21**, 082105 (2009).
- [20] J. T. McKeown, N. A. Roberts, J. D. Fowlkes, Y. Wu, T. LaGrange, B. W. Reed, G. H. Campbell, and P. D. Rack, Real-time observation of nanosecond liquid-phase assembly of nickel nanoparticles via pulsed-laser heating, *Langmuir* **28**, 17168 (2012).
- [21] S. H. Davis, Moving contact lines and rivulet instabilities. Part I: The static rivulet, *J. Fluid Mech.* **98**, 225 (1980).
- [22] D. Langbein, The shape and stability of liquid menisci at solid edges, *J. Fluid Mech.* **213**, 251 (1990).
- [23] J. A. Diez and L. Kondic, On the breakup of fluid films of finite and infinite extent, *Phys. Fluids* **19**, 072107 (2007).
- [24] L. Yang and G. M. Homsy, Capillary instabilities of liquid films inside a wedge, *Phys. Fluids* **19**, 044101 (2007).
- [25] F. Brochard-Wyart and C. Redon, Dynamics of liquid rim instabilities, *Langmuir* **8**, 2324 (1992).
- [26] K. Sekimoto, R. Oguma, and K. Kawasaki, Morphological Stability analysis of partial wetting, *Ann. Phys. (N.Y.)* **176**, 359 (1987).
- [27] H. A. Stone and L. G. Leal, Relaxation and breakup of an initially extended drop in an otherwise quiescent fluid, *J. Fluid Mech.* **198**, 399 (1989).
- [28] W. van Saarloos, Front propagation into unstable states, *Phys. Rep.* **386**, 29 (2003).
- [29] J. N. Israelachvili, *Intermolecular and Surface Forces*, 2nd ed. (Academic Press, New York, 1992).
- [30] A. González, J. A. Diez, Y. Wu, J. D. Fowlkes, P. D. Rack, and L. Kondic, Instability of liquid Cu films on a SiO₂ substrate, *Langmuir* **29**, 9378 (2013).
- [31] R. Balian and B. Duplantier, Electromagnetic waves near perfect conductors. II. Casimir effect, *Ann. Phys. (N.Y.)* **112**, 165 (1978).
- [32] I. Seric, S. Afkhami, and L. Kondic, Influence of thermal effects on stability of nanoscale films and filaments on thermally conductive substrates, *Phys. Fluids* **30**, 012109 (2018).
- [33] O. Heavens, *Optical Properties of Thin Solid Films*, Dover Books on Physics and Mathematical Physics (Dover Publications, New York, 1955).
- [34] W. Gale and T. Totemeier, *Smithells Metals Reference Book*, 8th ed. (Butterworth-Heinemann, London, 2004).
- [35] A. G. González, J. A. Diez, and M. Sellier, Inertial and dimensional effects on the instability of a thin film, *J. Fluid Mech.* **787**, 449 (2016).
- [36] N. Dong and L. Kondic, Instability of nanometric fluid films on a thermally conductive substrate, *Phys. Rev. Fluids* **1**, 063901 (2016).
- [37] J. Diez, A. González, D. Garfinkel, P. Rack, J. McKeown, and L. Kondic, Simultaneous decomposition and dewetting of nanoscale alloys: A comparison of experiment and theory, *Langmuir* **37**, 2575 (2021).
- [38] We note that for an increased laser energy, a single filament would melt as well; we choose the parameter so to illustrate clearly the effect of thermal crowding.